POLITECNICO DI TORINO
Repository ISTITUZIONALE

Numerical modelling of HTS response to magnetic field in perpendicular geometry

Original
Numerical modelling of HTS response to magnetic field in perpendicular geometry / Casciello, M., Calzolaio, C., De Stasio, M., Torsello, D., Savoldi, L., Laviano, F.. - In: CRYOGENICS. - ISSN 0011-2275. - 163:(2026), pp. 1-8. [10.1016/j.cryogenics.2026.104483]

Availability:
This version is available at: 11583/3016202 since: 2026-10-01T14:26:19Z

Publisher:
Elsevier

Published
DOI:10.1016/j.cryogenics.2026.104483

Terms of use:

This article is made available under terms and conditions as specified in the corresponding bibliographic description in the repository

Publisher copyright

(Article begins on next page)

26 November 2026

Cryogenics 163 (2026) 104483

Contents lists available at ScienceDirect

Cryogenics

journal homepage: www.elsevier.com/locate/cryogenics

Numerical modelling of HTS response to magnetic field in perpendicular geometry

Martina Casciello [a,b,*], Ciro Calzolaio [c], Mattia De Stasio [a,b], Daniele Torsello [b,d], Laura Savoldi [a,e], Francesco Laviano [b,d]

[a] Politecnico di Torino, Dipartimento di energia "Galileo Ferraris", Turin, Italy
[b] INFN, Turin, Italy
[c] Paul Scherrer Institute, Villigen, Switzerland
[d] Politecnico di Torino, Department of Applied Science and Technology, Turin, Italy
[e] INFN, Geneva, Italy

HIGHLIGHTS

- Coupled MOI and FEM modelling of HTS thin films.
- H–Φ formulation for magnetization of YBCO thin films.
- Quantitative validation of flux penetration in YBCO films.

ARTICLE INFO

Keywords:
High temperature superconductors
Magnetization
Critical state

ABSTRACT

Understanding the static and dynamic magnetic behaviour of High Temperature Superconductors (HTS) has significantly progressed thanks to the development of space- and time-resolved experimental techniques. Among them, Magneto-Optical Imaging (MOI) stands out as a non-destructive method capable of providing quantitative information on local magnetic flux distributions with micrometer-scale resolution. In this work, we investigate the magnetic response of high-quality $YBa_2Cu_3O_{7-x}$ thin films deposited on single crystal substrates (YSZ). MOI measurements were performed at different temperatures, in perpendicular geometry, i.e., with the applied field directed perpendicular to the HTS film. The MOI technique enables the direct reconstruction of the spatial distribution of supercurrent density and its dependence on the local magnetic flux density and temperature. To complement and interpret experimental observations, we developed numerical simulations based on an H-ϕ formulation in the FEM software COMSOL Multiphysics. This approach qualitatively captures the electrodynamic behaviour of the HTS film, including field penetration and current redistribution during applied field ramps. The agreement between simulated and measured magnetic field profiles is promising for the predictive capabilities of the numerical framework. The combined experimental and numerical analysis demonstrates that the model provides a reliable tool for investigating current limiting mechanisms, assessing sample inhomogeneities, and understanding the influence of microscopic defects, on the electromagnetic performance of HTS films. This achievement is also instrumental for predicting the behaviour of HTS tapes in high-field magnet designs.

1. Introduction

The non-uniform magnetic field and current density distribution inside superconductors must be considered to properly assess critical aspects in the design of high-field magnetic systems. Magneto-optical imaging (MOI) is a powerful technique to investigate the local magnetic field distribution over the surface of superconducting samples [1–5]. Compared to other magnetic field imaging methods, such as SQUID or Hall-probe scanning magnetometry [6], MOI provides real-time, spatially resolved measurements over a large surface area, enabling the direct observation of flux penetration and current redistribution processes [7,8]. The technique is based on the Faraday effect [9]: a ferromagnetic indicator film placed on top of the superconductor modifies

* Corresponding author at: Politecnico di Torino, Dipartimento di energia "Galileo Ferraris", Turin, Italy.
Email address: martina.casciello@polito.it (M. Casciello).

https://doi.org/10.1016/j.cryogenics.2026.104483
Received 24 April 2026; Received in revised form 9 September 2026; Accepted 16 September 2026
Available online 18 September 2026
0011-2275/© 2026 The Author(s). Published by Elsevier Ltd. This is an open access article under the CC BY license (http://creativecommons.org/licenses/by/4.0/).

its local magnetization in response to the local magnetic field, resulting in a modulation of the intensity of polarized light. After a proper calibration procedure, the measured light intensity can be converted into the perpendicular component of the magnetic induction. For thin superconducting samples, this information is sufficient to reconstruct the in-plane current density distribution through the numerical inversion of the Biot–Savart law [10].

Despite its advantages, the quantitative interpretation of MOI measurements is not trivial. In particular, the indicator film can be affected not only by the perpendicular magnetic field component, but also by in-plane contributions generated by the supercurrents [11,12]. These effects may introduce artefacts in the reconstructed current density distribution if they are not properly taken into account [13]. Nevertheless, when combined with appropriate calibration and inversion procedures, MOI remains a powerful tool for the analysis of local electrodynamic properties in superconductors.

In parallel, numerical modelling plays a crucial role in the interpretation of superconducting behaviour [14]. The electromagnetic response of high-temperature superconductors is typically described by nonlinear constitutive relations, such as the power-law E-J relation, which accounts for flux creep. Among the available numerical approaches, the finite element method (FEM) has proven to be particularly effective for solving Maxwell's equations in superconducting systems. In this context, the so-called H-formulation, which solves for the magnetic field vector **H** in the whole domain, has been widely used due to its robustness and ease of implementation [15,16], and has been successfully applied to the modelling of bulk magnetization [17–19]. However, only limited number of studies have addressed the FEM simulation of very thin superconducting films.

The H-formulation, in particular, presents some limitations, especially related to the need to solve for a full vector field also in non-conducting regions, which increases computational cost and may degrade numerical conditioning. Mixed formulations, such as the H-Φ formulation [22], overcome these limitations by coupling the magnetic field in superconducting regions with a scalar (**Φ**) in current-free domains, thereby reducing the number of degrees of freedom while preserving accuracy.

In this work, we combine Magneto-Optical Imaging (MOI) measurements with FEM simulations to investigate the magnetic response of $YBa_2Cu_3O_{7-x}$ (YBCO) thin films under a perpendicular magnetic field. Although MOI and FEM numerical modelling are well-established techniques, a direct and quantitative integration of the two remains insufficiently validated. Here, we address this gap by establishing a consistent framework that enables a direct comparison between experimental observations and FEM simulations.

In this paper, Chapter 2 introduces the MOI technique used for the experimental analysis. Chapter 3 presents the numerical model, where the H–Φ formulation is adopted as a suitable compromise between computational efficiency and accuracy [22,23]. In Chapter 4, we report the experimental results obtained on a reference film and on a film of the same material containing a region subjected to heavy-ion irradiation, enabling the assessment of the model's capability to reproduce flux penetration, current distribution, and the effects of engineered pinning centres. The experimental results are then systematically compared with the corresponding numerical simulations, with a discussion of the observed discrepancies.

2. Experimental set-up

The core of the experimental apparatus consists of an optical microscope integrated with a highly sensitive magneto-optical indicator film, a Bismuth-doped Iron Garnet $Bi_3(Fe,Ga)_5O_{12}$ (BIG) grown via liquid phase epitaxy on a transparent single crystal Gadolinium Gallium (GGG) substrate [24]. As shown in Fig. 1, a light beam originating from a mercury (Hg) lamp is collimated by a bi-convex lens, linearly polarized, and directed through a beam-splitter and an objective lens onto the surface

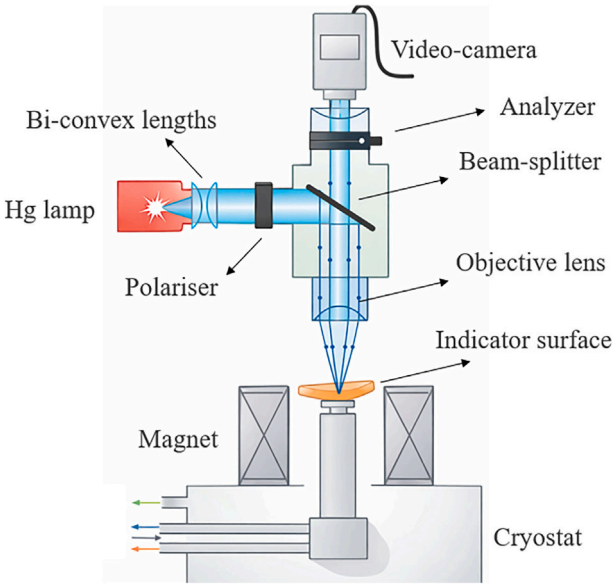


Fig. 1. Scheme of the MOI experimental set-up.

of the indicator. To maximize the signal-to-noise ratio, the indicator is engineered with a reflective backing in direct physical contact with the sample. This mirror forces the light beam to be refracted twice through the active material, effectively doubling the specific Faraday rotation [25].

The sample-indicator assembly is housed inside an optical cryostat (allowing precise temperature control ranging from 3.5 K to 350 K) and is subjected to a uniform perpendicular magnetic field up to 0.2 T generated by a water-cooled electromagnet. The returning light passes through a rotating analyzer, conventionally set to a nearly crossed position (typically 2 to 3 degrees off the crossed condition), before being focused onto a digital CCD camera, as shown in Fig. 1. Consequently, the variation in the local out-of-plane magnetic field induces local Faraday rotations that are translated into light intensity fluctuations mapped across the CCD matrix. The sample must satisfy some geometric constraints: it must be fully contained within the imaged field of view together with enough surrounding stray field, and it must fit within the area of good thermal contact on the cryostat's cold finger, which has a diameter of about 1 cm.

In this work, a magneto-optical indicator film with in-plane magnetization was placed directly on top of the superconducting sample.

Two superconducting samples were investigated: an as-grown YBCO film and a second film of the same material containing a region subjected to heavy-ion irradiation, in order to see what the effect of the engineered pinning landscape is at the same time. Both samples were placed inside the optical cryostat, in close thermal contact with the cold finger, and exposed to a magnetic field applied perpendicular to the sample surface. For each measurement, data acquisition began only once isothermal conditions were reached (temperature stability better than 10 mK), ensuring that the sample temperature could be treated as constant and spatially uniform throughout each field sweep. A sequence of images was acquired during the magnetic field ramp, allowing the observation of flux penetration and hysteresis effects.

The perpendicular component of the magnetic field was extracted from the calibrated images. Subsequently, the in-plane current density distribution was reconstructed using numerical inversion of the Biot-Savart law based on FFT methods [10]. This FFT-based inversion assumes a periodic domain, so it is naturally prone to spurious current leakage beyond the physical edges of the sample. Two corrections are used here to limit this effect. First, the field of view is chosen large enough to include the whole sample plus its surrounding stray field;

any remaining high-frequency noise is then removed with a Hanning window filter in k-space. Second, close to the sample edges the in-plane magnetic field from the supercurrents becomes as large as the perpendicular component B_z. To correct for this, the in-plane field is estimated from the current density at each iteration (via the Biot–Savart law) and used to correct the calibrated B_z map.

The magnetic field induced by the current density flowing in the sample is given by:

$$\mu_0 \mathbf{H}_{\text{ind}}(\mathbf{r}) = \frac{\mu_0}{4\pi} \int \frac{\mathbf{J}(\mathbf{r}') \wedge (\mathbf{r} - \mathbf{r}')}{|\mathbf{r} - \mathbf{r}'|^3} d^3 r' \tag{1}$$

Under the assumption of a flat and thin sample, and imposing $\nabla \cdot \mathbf{J} = 0$, the two-dimensional FFT of this relation reduces to a solvable linear system for the in-plane current density components:

$$\begin{cases} \mu_0 \tilde{H}_z(k_x, k_y, h) = i \dfrac{\mu_0}{2} \tilde{J}_x(k_x, k_y) \dfrac{e^{-hk}}{k_y} \sinh\left(\dfrac{d}{2} k\right) \\ \tilde{J}_x(k_x, k_y) = -\tilde{J}_y(k_x, k_y) \dfrac{k_x}{k_y} \end{cases} \tag{2}$$

with $k = \sqrt{k_x^2 + k_y^2}$.

This approach allows the simultaneous evaluation of the magnetic field distribution and current density evolution, providing a direct comparison with the numerical simulations.

3. Numerical model

The electromagnetic behaviour of the superconducting thin films was simulated using a FEM approach. Due to the strongly nonlinear electrodynamics of type-II superconductors, an appropriate formulation is required to accurately describe flux penetration and current redistribution. Different electromagnetic formulations were considered, including the T–A formulation, the full **H** formulation, and the mixed **H**–Φ formulation. The T–A formulation, which uses the current vector potential **T** and the magnetic vector potential **A** as state variables, provides high computational efficiency, particularly for computing integrated quantities such as AC and magnetization losses in coated conductors [20,21], owing to its representation of the superconducting layer as an infinitely thin current sheet. In this work, however, the goal is a direct, spatially-resolved comparison between simulated and MOI-measured local field and current density distributions, resolved explicitly with a mapped mesh of 3 elements across the thickness; for this purpose, a formulation resolving the real film geometry is more directly suited, and the H–Φ formulation was adopted as an effective compromise between this accuracy and computational efficiency. The full H formulation offers high accuracy but requires solving the magnetic field in the entire computational domain, resulting in high computational cost. In this work, the H–Φ formulation was selected to reduce effectively the degrees of freedom in the electromagnetic simulation. In fact, as cited before, it confines the magnetic vector **H** to superconducting region and utilizes a magnetic scalar potential ϕ in current-free domain [22,26].

In this study, finite element simulation of the magnetization process were performed using Comsol Multiphysics. The model is fully three-dimensional. The superconducting film is defined as a real 3D domain with the actual physical thickness and lateral dimensions of the patterned sample (800 μm × 0.25 mm × 200 nm for the reference film, 900 μm × 0.2 mm × 400 nm for the irradiated one).

In the superconducting regions, the system is governed by the standard **H**-formulation expression:

$$\nabla \times (\rho \nabla \times \mathbf{H}) = -\mu_0 \frac{d\mathbf{H}}{dt} \tag{3}$$

where ρ represents the non-linear resistivity according to the power law:

$$\rho = \frac{E_c}{J_c(||\mathbf{B}||)} \left(\frac{||\mathbf{J}||}{J_c(||\mathbf{B}||)} \right)^{n-1} \tag{4}$$

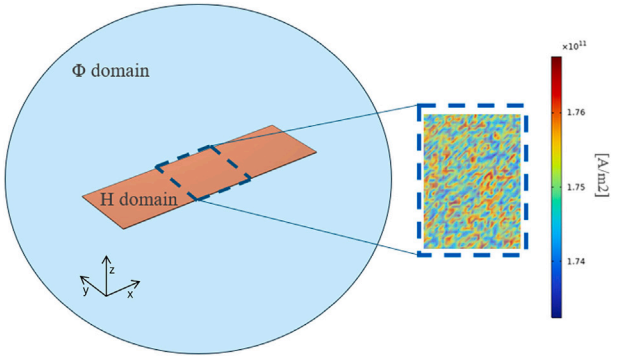


Fig. 2. Representation of the H and Φ domains, and the distribution of the critical current density in the YBCO film.

In the non-conducting region, the magnetic field **h** is obtained directly from the potential via:

$$\mathbf{h} = -\nabla \phi \tag{5}$$

which mathematically enforces the zero current density. By applying the divergence-free condition from the Maxwell's equations $\nabla \cdot B = 0$ and assuming $\mu_0 \mathbf{H}$, the governing equation in the air domains simplifies to Laplace's equation (Fig. 2):

$$\nabla \cdot \nabla \phi = 0 \tag{6}$$

The tape was discretized using a mapped mesh with three elements across its thickness to accurately capture the current distribution. A free tetrahedral mesh was employed in the surrounding air domain. Real superconducting films are never perfectly homogeneous, due to local variations in thickness and pinning landscape inherent to the growth and patterning process. To account for this physical inhomogeneity, the critical current density was spatially distributed using a Gaussian variation of 2% around the nominal value, consistent in order of magnitude with the point-to-point dispersion observed in the plateau region of the experimentally reconstructed current density profiles. This is a second-order correction: the macroscopic critical-state behaviour remains entirely governed by the nominal $J_c(B)$ constitutive law of Eq. (2).

In order to verify that the simulated results are not sensitive to the specific amplitude chosen for this perturbation, a dedicated sensitivity analysis was additionally carried out, extending the imposed dispersion beyond the nominal 2% up to 5% and 10%. For each dispersion level, 20 independent random configurations of the Gaussian Jc map were generated. For every level, the mean and standard deviation of the extracted J(x) profile were computed pointwise across the 20 realizations (Fig. 3a), and the maximum pointwise relative deviation from the reference simulation with spatially uniform Jc (0% dispersion, baseline case) was evaluated (Fig. 3b). This maximum-error metric was then compared across the three dispersion levels to quantify how the sensitivity of the simulated response scales with the amplitude of the imposed Jc dispersion. The analysis shows that the maximum pointwise deviation from the baseline remains below 10% even for the highest dispersion level considered. This confirms that the simulated response is not significantly affected by the amplitude of the imposed spatial Jc dispersion, supporting the robustness of the 2% value adopted throughout this work.

4. Results and discussion

In this section, the experimental measurement and the simulations are compared for both the reference as-grown film and for the partially irradiated one.

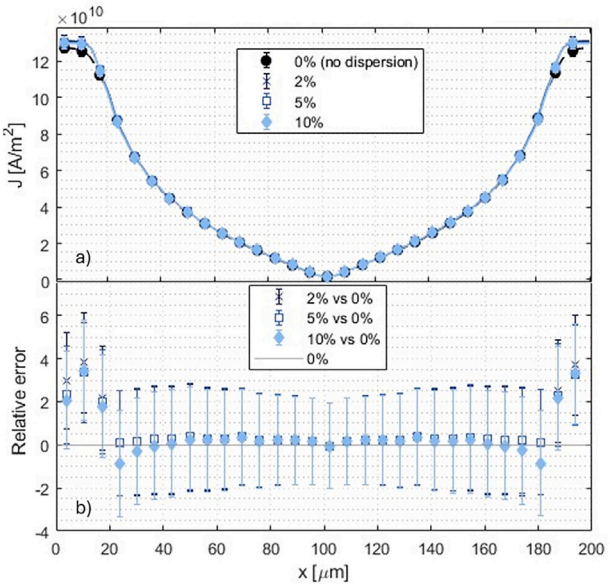


Fig. 3. (a) Simulated current density profile J(x) across the sample width, for different levels of Gaussian spatial dispersion imposed on Jc (0%, 2%, 5%, 10%). (b) Relative deviation of the dispersed cases with respect to the spatially uniform baseline (0% dispersion).

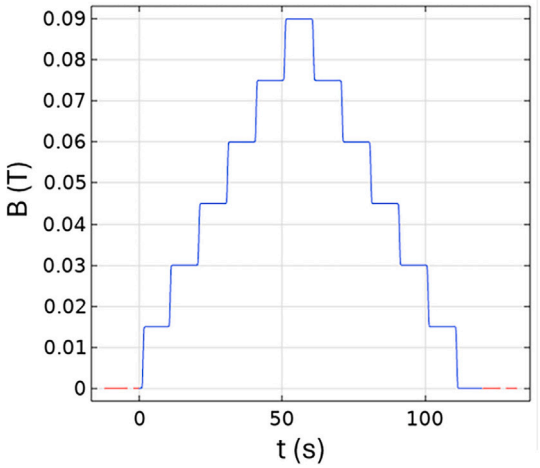


Fig. 4. Applied magnetic field during the test of the reference thin film.

4.1. Experimental results of the reference film

MOI measurements were first performed on a reference YBCO thin film under perpendicular magnetic field. The YBCO film was patterned by standard photolithography to a size of 800 μm × 0.25 mm, with a thickness of 200 nm.

The applied magnetic field, shown in Fig. 4, was increased stepwise up to 0.09 T and subsequently reduced to zero in order to investigate flux penetration and flux trapping phenomena.

Fig. 5 shows the experimental results for the magnetic field distribution at selected time steps during the field ramp. At low applied field (Fig. 5 (a)), the magnetic flux remains confined near the edges of the sample, due to vortex pinning and effective screening by shielding currents. As the applied field increases (Fig. 5 (b), (c)), magnetic flux progressively penetrates toward the centre of the film, forming a characteristic cushion-like pattern [27].

During the decreasing field stage (Fig. 5 (d)), the magnetic field distribution changes significantly and part of the flux remains trapped

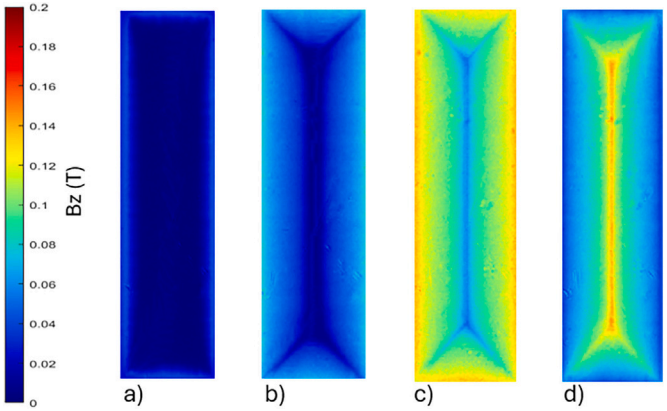


Fig. 5. Measured perpendicular magnetic field distribution with an applied external field of 0.015 T (a), 0.045 T (b), 0.09 T (c), and 0.045 T during the ramp down (d).

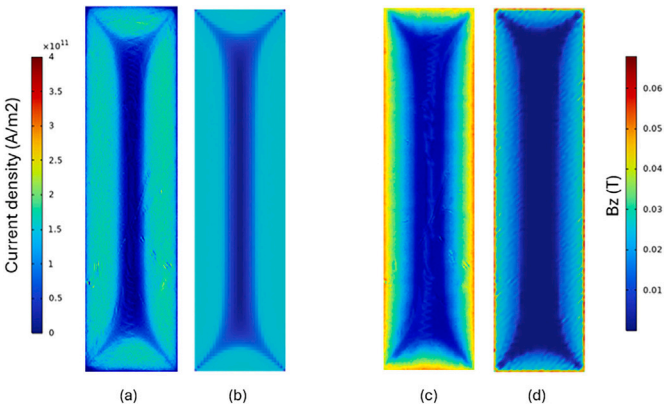


Fig. 6. Comparison between the experimental ((a),(c)) and simulated ((b),(d)) distributions respectively of the current density ((a),(b)) and the magnetic field ((c),(d)) at an applied magnetic field of 0.04 T. The colour scale is shared between (a) and (b), and between (c) and (d), to allow direct visual comparison between experiment and simulation. (For interpretation of the references to colour in this Figure legend, the reader is referred to the web version of this article.)

inside the sample. This behaviour is consistent with flux pinning and hysteretic response typical of hard type-II superconductors.

4.1.1. Comparison with numerical model

The experimental magnetic field maps were compared with numerical simulations obtained using the **H**-Φ formulation. Fig. 6 shows the comparison between measured and simulated magnetic field distributions.

The simulation reproduces the main spatial features of flux penetration. In both experiment and simulation, the magnetic field is concentrated near the edges and decreases toward the central region. The shape of the penetration front and the overall field distribution are in good agreement.

Minor discrepancies are observed near the edges, which can be attributed to experimental noise and defects in the magneto-optical indicator.

The comparison between experimental and simulated results is further assessed through profiles of the magnetic field and current density extracted along the midline crossing the tape, as shown in Fig. 7.

The magnetic field profiles exhibit the expected behaviour, with lower values in the central region and higher values near the edges, corresponding to the flux penetration fronts. The simulated curves closely

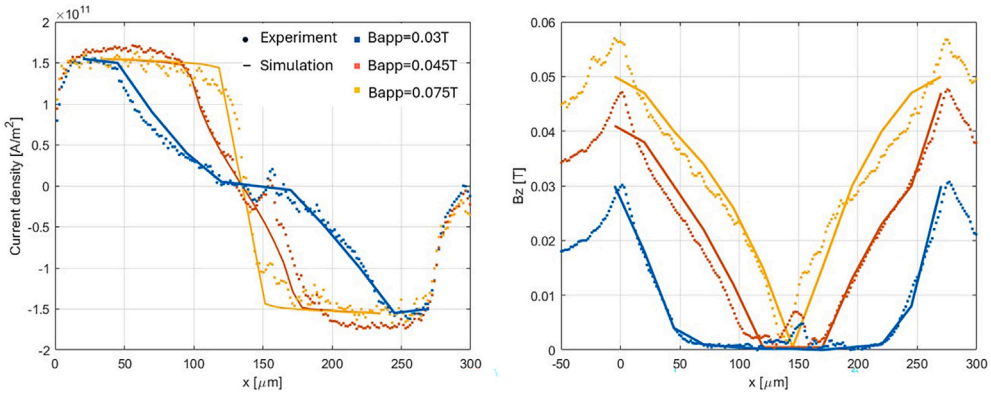


Fig. 7. Current density and magnetic field profiles that compare experimental data (markers) and simulations (solid lines).

Table 1
Critical currents of the two regions of the YBCO film.

	Jc	Unit
As-grown	$1.75 \cdot 10^{1}1 \pm 2\%$	A/m^2
Irradiated	$2.1 \cdot 10^{1}1 \pm 2\%$	A/m^2

follow the experimental data for different applied magnetic fields, capturing both the magnitude and the spatial variation of the field distribution. Some discrepancies can be observed, particularly near the edges and in regions with steep gradients. In these regions, the current density is expected to rise sharply; the simulation mesh was not locally refined at the sample edges, while the experimental reconstruction includes a filtering step in the inversion algorithm that smooths the sharpest features. This resolution limitation, present on both sides, is considered the main origin of the observed deviation. These deviations remain quantitatively small and confined to the edges and steepest-gradient regions, with good agreement observed over the rest of the profile.

Similarly, the current density profiles show good agreement between experiment and simulation. The current is mainly concentrated near the penetration fronts, where shielding currents oppose the applied magnetic field, while it decreases toward the centre of the sample.

Some discrepancies can be observed, particularly near the edges and in regions with steep gradients.

4.2. Experimental measurement of the irradiated sample

A second experiment was performed on a partially irradiated YBCO thin film in order to investigate the effect of artificial pinning centres.

The sample was patterned by standard photolithography and a laser to a size of 900 um × 0.2 mm with a thickness of 400 nm. In this case, 350 μm of the total length was irradiated with Au ions at an energy of 250 MeV at low fluence ($\sim 5 \cdot 10^{10}$ ions/cm^2). Heavy-ion irradiation introduces columnar defects that enhance vortex pinning and modify flux penetration [28,29]. The irradiated region exhibits a 20% increase in the critical current peak, as shown in Table 1.

For this second experiment, a slower ramp with $1.5 \cdot 10^{-5}$ T steps was applied using the external magnet, up to a peak of 0.18 T, and then ramped back down to 0, as shown in Fig. 8. Anyway, the ramp velocity does not influence the final magnetization.

Fig. 9 illustrates the magnetization process through a sequence of magnetic flux density maps during both the ramp-up and ramp-down of the applied magnetic field. The upper region is the irradiated one, and the lower is the virgin one. In the top row, as the applied field B_{App} increases from 0.03 T to 0.18 T, flux progressively penetrates the sample from the edges toward the centre. The characteristic "roof-top" or Bean-like profile becomes more pronounced, with higher B_z values

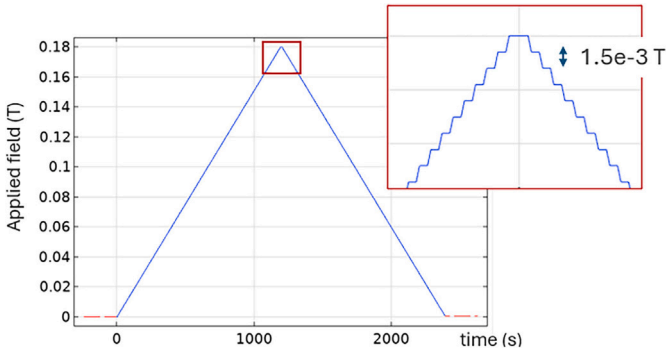


Fig. 8. Applied magnetic field during testing of the irradiated film.

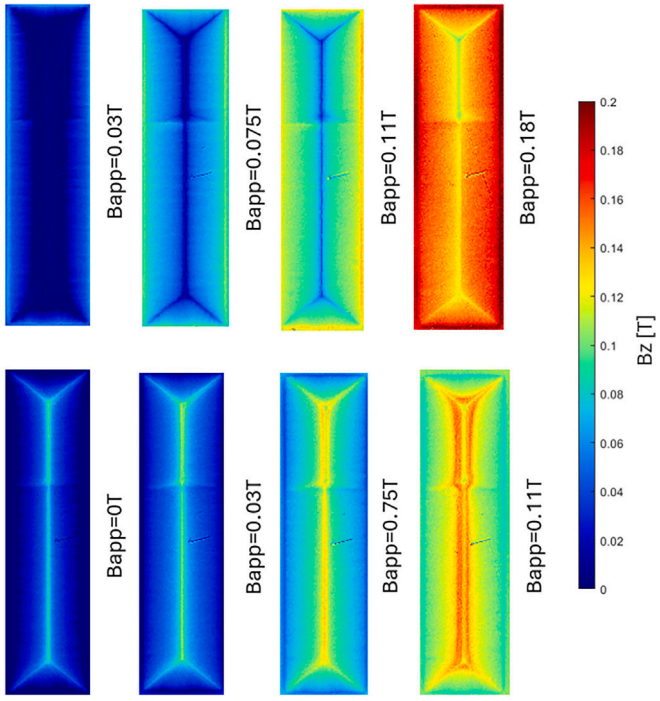


Fig. 9. Measured magnetic flux density B_z maps, illustrating the magnetization process. The colour scale is shared between the figures, to allow direct visual comparison. (For interpretation of the references to colour in this Figure legend, the reader is referred to the web version of this article.)

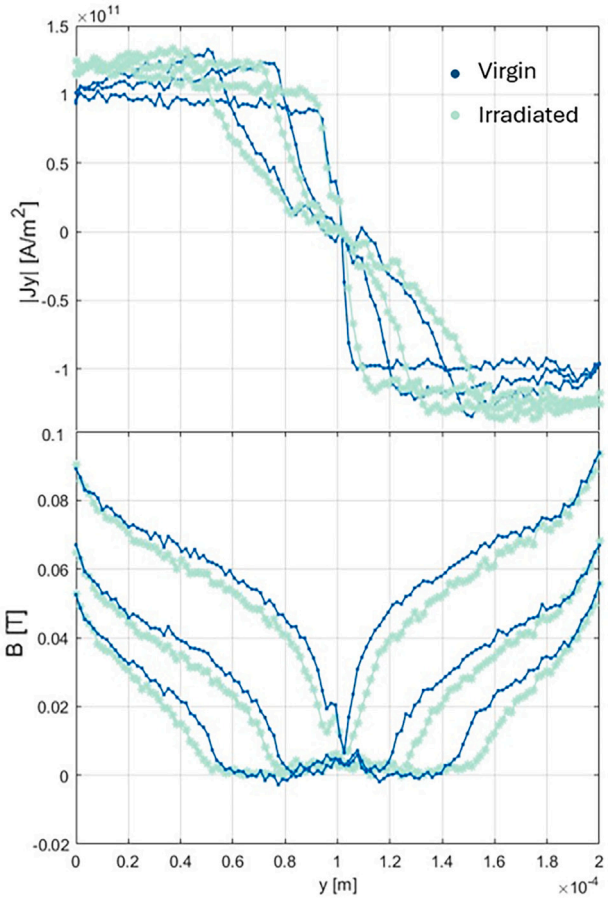


Fig. 10. Comparison of the current density and magnetic field distribution of the as-grown region and irradiated region of the film with an increasing external magnetic fields of 0.03 T, 0.07 T and 0.1 T.

(yellow–red) indicating deeper flux penetration and stronger current flow near the edges.

In the bottom row, during the ramp-down back to zero field, a clear hysteretic behaviour is observed. Even when $B_{app} = 0$, a non-zero trapped flux remains inside the sample. The flux distribution becomes more concentrated in the central region, reflecting the redistribution of vortices as the external field is reduced.

The irradiated region exhibits a wider flux-free region and steeper magnetic field gradients. This behaviour can be attributed to the different nature of vortex pinning in the two regions. The irradiated region contains columnar defects that provide strong, correlated pinning centres, keeping the current path regular and well-defined as the field increases. The virgin region relies instead on the weaker, randomly distributed pinning typical of the as-grown film.

Fig. 10 compares the current density along the y direction (Jy) and the magnetic field profiles along the y-direction for the virgin and irradiated films.

In the top panel, the current density profiles exhibit the typical plateau associated with the critical state. The irradiated sample shows a slightly reduced peak current density and a smoother transition near the edges of the plateau, indicating the effect of columnar defects in modifying the critical current distribution.

In the bottom panel, the magnetic field profiles reflect these differences. The irradiated film displays a more gradual spatial variation of B, with reduced field gradients near the edges, consistent with the modified current density.

4.3. Comparison with numerical model

A comparison between the experimental data and the numerical simulations is reported in Figs. 11 and 12. The spatial distributions of the current density and magnetic field (Fig. 11) show that the model is able to reproduce the main features of the critical state, namely the enhanced current density near the sample edges and the corresponding magnetic field profile characterized by a minimum at the centre.

However, noticeable differences emerge when inspecting the experimental maps. In particular, the current density distribution appears less homogeneous and slightly asymmetric, with local fluctuations that are absent in the simulations. Similarly, the magnetic field maps exhibit a smoother spatial variation and reduced contrast compared to the idealized numerical results. These discrepancies can be attributed to intrinsic sample inhomogeneities and pinning landscape variations not represented by the 2% Gaussian variation included in the model.

A more quantitative comparison is provided by the line profiles shown in Fig. 11. While the overall agreement between experiment and simulation is satisfactory, the experimental curves display rounded transitions and systematically lower peak values of the current density.

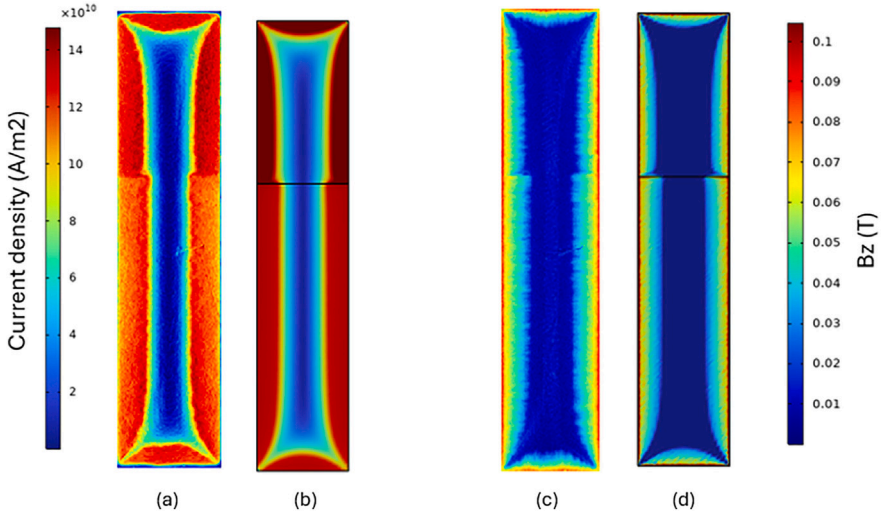


Fig. 11. Comparison between the experimental and simulated distributions respectively of the current density ((a),(b)) and the magnetic field ((c),(d)) with an applied magnetic field of 0.04 T. The colour scale is shared between (a) and (b), and between (c) and (d), to allow direct visual comparison between experiment and simulation. (For interpretation of the references to colour in this Figure legend, the reader is referred to the web version of this article.)

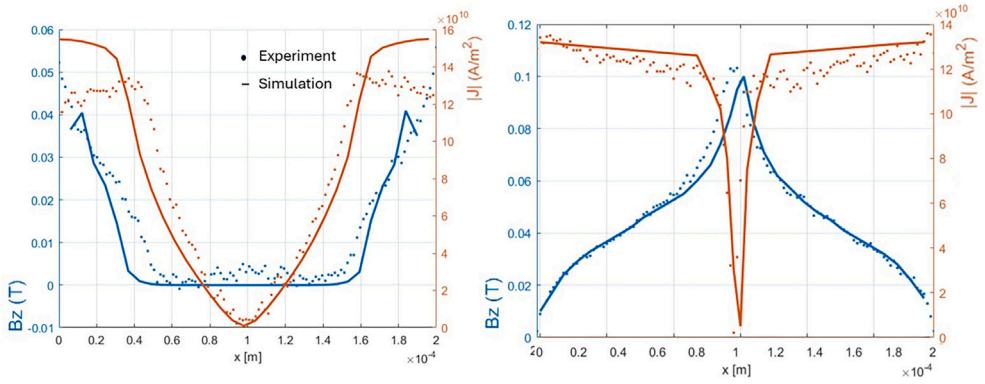


Fig. 12. Line profiles of the magnetic field B_z (left axis) and current density J_y (right axis) along the irradiated region across the sample width, comparing experimental data (markers) with simulations (solid lines).

5. Conclusions

In this work, we have combined MOI and finite element simulations to investigate the magnetic response of YBCO thin films under perpendicular magnetic field. The spatially resolved B_z maps obtained by MOI were converted into current density distributions, enabling a direct comparison with numerical results. The simulations reproduce the main features of flux penetration and current distribution within the critical state framework, showing good agreement with the experimental data. In particular, the **H**–Φ formulation was found to provide an effective compromise between computational efficiency and accuracy, overcoming some of the limitations of the conventional **H**-formulation. Deviations between experiments and simulations, such as smoother profiles and reduced peak current densities, can be attributed to flux creep, and sample inhomogeneities which are not fully captured by the model. Finally, the approach was validated on both pristine and ion-irradiated samples, demonstrating its capability to describe the effects of engineered pinning centres on flux penetration. Preliminary PPMS magnetometry measurements on these samples yield critical current density values in good agreement with those obtained by MOI and FEM, providing an independent cross-check that will be discussed in detail in a forthcoming, dedicated publication.

These results highlight the potential of combining MOI and advanced numerical modelling into a powerful tool for the quantitative analysis and design of superconducting materials.

CRediT authorship contribution statement

Martina Casciello: Writing – original draft, Visualization, Software, Methodology, Investigation, Data curation. **Ciro Calzolaio:** Writing – review & editing, Supervision, Resources, Methodology. **Mattia De Stasio:** Writing – review & editing, Software, Methodology. **Daniele Torsello:** Writing – review & editing, Supervision. **Laura Savoldi:** Writing – review & editing, Supervision. **Francesco Laviano:** Writing – review & editing, Supervision, Methodology, Investigation, Data curation, Conceptualization.

Declaration of competing interest

The authors declare the following financial interests/personal relationships which may be considered as potential competing interests:

Martina Casciello reports that administrative support and writing assistance were provided by Paul Scherrer Institute PSI. If there are other authors, they declare that they have no known competing financial interests or personal relationships that could have appeared to influence the work reported in this paper.

Data availability

Data will be made available on request.

References

[1] Jooss C, et al., Magneto-optical studies of current distributions in high T_c superconductors. Rep Prog Phys 2013:651–788.
[2] Laviano F, et al., Evidence of vortex curvature and anisotropic pinning in superconducting films by quantitative magneto-optics. Phys Rev B 2003;68.
[3] Kim YB. Magnetization and critical supercurrents. Phys Rev 1963;129.
[4] Koblischka M, et al., Magneto-optical investigations of superconductors. Supercond Sci Technol 1995;8.
[5] Johansen TH, Shantsev DV, (editors). Magneto-optical imaging. NATO science series. Vol. 142. Springer; 1999.
[6] Oral A, et al., Scanning hall probe microscopy of superconductors and magnetic materials. Appl Phys Lett 1996;69.
[7] Forkl A, et al., Magneto-optical investigation of flux penetration in $Y_1 Ba_2 Cu_3 O_7$ thin film. Appl Phys Lett 1990;57:1067–9.
[8] Johansen TH, et al., Direct observation of the currend distribution in thin superconducting strips using magneto-optic imaging. Phys Rev B 1996;54:16264.
[9] Faraday M. "Experimental researches in electricity—nineteenth series". Philos Trans R Soc Lond 1846;136:1–20.
[10] Laviano F, et al., "An improved method for quantitative magneto-optical analysis of superconductors". Supercond Sci Technol 2003;16:71–9.
[11] Brandt EH, et al., Type-II superconducting strip in perpendicular magnetic field. Lett J Explor Front Phys 1995;22.
[12] Brandt E. Determination of currents in flat superconductors. Phys Rev B 1992;46.
[13] Gurevich A, et al., Nonlinear transport current flow in superconductors with planar obstacles. Phys Rev B 2000;62.
[14] Sirois F, et al., Potential and limits of numerical modelling for supporting the development of HTS devices. Supercond Sci Technol 2015;28.
[15] Shen B, et al., Overview of H-Formulation: a versatile tool for modeling electromagnetics in high-temperature superconductor applications. IEEE Trans Appl Supercond 2020;8.
[16] Shen B, et al., Review of the AC loss computation for HTS using H formulation. Supercond Sci Technol 2020;33.
[17] Zou J, et al., "Numerical modelling and comparison of MgB2bulks fabricated by HIP and infiltration growth. Supercond Sci Technol 2015;28.
[18] Hong Z, et al., Numerical solution of critical state in superconductivity by finite element software. Supercond Sci Technol 2006;19:1246–52.
[19] Ainslie MD. Modelling of bulk superconductor magnetization. Suupercond Sci Technol 2015;28.
[20] Wang Y. Study of the magnetization loss of CORC® cables using a 3D T-A formulation. Supercond Sci Technol 2019;32.
[21] De Marzi G, et al., An analytical model for predicting the magnetization loss in HTS sector-shaped conductors for fusion. Supercond Sci Technol 2024;37(12):125007.
[22] Arsenault A, et al., Implementation of the h-Φ formulation in COMSOL multiphysics for simulating the magnetization of bulk superconductors and comparison with the H-Formulation. IEEE Trans Appl Supercond 2020;31.
[23] Huber F, et al., The T-A formulation: an efficient approach to model the macroscopic electromagnetic behaviour of HTS coated conductor applications. Supercond Sci Technol 2022;35.
[24] Helseth LE, et al., Faraday rotation and sensitivity of (100) bismuth-substituted ferrite garnet films. Phys Rev B 2002;66.
[25] Helseth LE, et al., Faraday rotation spectra of bismuth-substituted ferrite garnet films with in-plane magnetization. Phys Rev B 2001;64.

[26] Arsenault A, et al., Efficient modeling of high-temperature superconductors surrounded by magnetic components using a reduced h–Φ formulation. IEEE Trans Appl Supercond 2021;NN.
[27] Schuster T, et al., Current and field pattern in rectangular and inhomogeneous superconductors. Phys Rev B 1995;52:10375.
[28] Strickland NM, et al., Effective low-temperature flux pinning by au ion irradiation in HTS coated conductors. IEEE Trans Appl Supercond 2015;25.
[29] Petrykin V, et al., Enhancement of 2G-HTS wire performance in strong magnetic fields through heavy ion irradiation. Supercond Sci Technol 2025;38.